SPECIAL
DYNAMO/CINDY/AMIE/LASP
COLLECTION

Hydrometeor Storage and Advection Effects in DYNAMO Budget Analyses

RICHARD H. JOHNSON,[a] PAUL E. CIESIELSKI,[a] AND WAYNE H. SCHUBERT[a]

[a] *Department of Atmospheric Science, Colorado State University, Fort Collins, Colorado*

(Manuscript received 5 October 2021, in final form 14 December 2021)

ABSTRACT: The Dynamics of the Madden–Julian Oscillation (MJO) (DYNAMO) field campaign over the central Indian Ocean captured three strong MJO events during October–December 2011. Using the conventional budget approach of Yanai et al. surface rainfall P_0 is computed as a residual from the vertically integrated form of the moisture budget equation. This budget-derived P_0 is spatially averaged over the Gan Island NCAR S-PolKa radar domain and compared with rainfall estimates from the radar itself. To isolate the MJO signal, these rainfall time series are low-pass (LP) filtered and a three-MJO composite is created based on the time of maximum LP-filtered S-PolKa rainfall for each event. A comparison of the two composite rainfall estimates shows that the budget rainfall overestimates the radar rainfall by ~15% in the MJO buildup stage and underestimates radar rainfall by ~8% in the MJO decay stage. These rainfall differences suggest that hydrometeor (clouds and rain) storage and advection effects, which are neglected in the budget approach, are likely significant. Satellite and ground-based observations are used to investigate these hydrometeor storage and advection effects. While the findings are qualitatively consistent with expectations from theory, they fall short of explaining their full magnitude, suggesting even more refined experimental designs and measurements will be needed to adequately address this issue.

KEYWORDS: Convection; Water budget/balance; Numerical analysis/modeling

1. Introduction

The methodology to diagnose the properties of tropical cloud clusters introduced by Yanai et al. (1973) has been utilized in numerous studies. This procedure has been valuable in many applications, yet continued advances in measurement technology motivate the use of a more accurate treatment of thermodynamics in such budget analyses. In the Yanai et al. diagnostic framework, referred to here as the conventional budget method (CBM), moist static energy is assumed to be conserved, apart from radiative effects. It is also assumed that the latent heat of condensation L is constant, such that important physical effects of ice (freezing, melting, deposition, sublimation) are neglected. In addition, the storage and advection of cloud condensate and precipitating hydrometeors are not considered. Under certain conditions, these effects can be important (Peixoto and Oort 1992).

These complicating factors associated with the conventional budget approach can be interpreted physically in the following way as they relate to MJO convection. First, with respect to storage, as the cloud field increases during the developing phase of the MJO, cloud condensate is "stored" in the atmosphere rather than precipitating out immediately. The reverse effect holds true during the decaying phase. Second, advection in deep convective systems can transport hydrometeors into or out of a sampling volume, which can also contribute to errors in traditional budgets that exclude these effects. Johnson (1980) estimated that the neglect of cloud storage effects resulted in errors on the order of 20% in the column-integrated moisture budget during periods of rapidly evolving cloud fields in Atlantic tropical easterly waves. On even shorter time scales, cloud storage and hydrometeor advection effects are particularly important, such as in the case of diurnal thunderstorm development (McNab and Betts 1978) and squall-line evolution (Gallus and Johnson 1991).

Ooyama (1990, 2001) proposed a very accurate form of moist thermodynamics for use in tropical models, namely, one that includes hydrometeor storage and advective effects. His formulation of moist thermodynamics is not limited to modeling studies but can also be used in heat and moisture budget studies (Schubert et al. 2018). With the advent of radiosondes with GPS-derived winds and the recent availability of certain satellite data products, this more accurate treatment of moist thermodynamics provides the opportunity to refine diagnostic analyses of a wide range of precipitation systems. As a preliminary effort toward this end, hydrometeor storage and advective effects in thermodynamic budgets are evaluated using observations from the 2011/12 Dynamics of the MJO (DYNAMO) field campaign. The strategy is to compare CBM-diagnosed rainfall-rate estimates with independent estimates of those quantities obtained from ground- and space-based remote sensing platforms. While the lack of precise measurements of hydrometeor storage and advection in

Corresponding author: Richard H. Johnson, richard.h.johnson@colostate.edu

DOI: 10.1175/JAS-D-21-0266.1

DYNAMO precipitation systems limits the extent to which these processes can be accurately evaluated, these comparisons yield insight into their aggregate impacts on the thermodynamic budgets.

2. Data and methods

a. Data

Observations used in this study are from the DYNAMO field campaign, conducted from October 2011 through March 2012 over the central Indian Ocean (Yoneyama et al. 2013). DYNAMO was designed to investigate processes associated with the initiation of the Madden–Julian oscillation (MJO; Madden and Julian 1971). The sounding network established during DYNAMO was composed of two quadrilateral arrays straddling the equator (Fig. 1). This network forms the basis of our study, with a focus on the period 2 October–31 December when the overall network was most complete and four to eight sounding launches per day were achieved (Ciesielski et al. 2014). Three prominent MJOs occurred in the DYNAMO domain during this 3-month period (Gottschalck et al. 2013). The Atmospheric Radiation Measurement (ARM) program operated a supersite located at Gan Island (0.69°S, 73.2°E) as part of the ARM MJO Investigation Experiment (AMIE). This site had multiple radars and radiometers, as well as 8-day^{-1} sounding observations. In addition, the National Center for Atmospheric Research S-band dual polarization Doppler radar S-PolKa (SPOL) was deployed on Gan Island. SPOL provides rainfall-rate estimates that can be compared to those determined from atmospheric sounding budgets. The sounding and radar datasets were quality controlled and bias corrected in connection with a special effort to create a DYNAMO legacy dataset (Ciesielski et al. 2014; Xu et al. 2015).

Other data used in this study include cloud liquid and ice paths as well as fractional cloud amount from the Clouds and the Earth's Radiant Energy System (CERES) product at 3-h resolution on a 1° grid (Wielicki et al. 1996). Also used are liquid and ice water path (LWP and IWP) estimates from the Pacific Northwest National Laboratory (PNNL) Combined Retrieval (CombRet) product based on cloud profiles, provided primarily by a zenith-pointing Doppler Ka-band cloud radar (KAZR) merged with SPOL observations, and incorporating sounding-based thermodynamic measurements at Gan Island (Feng et al. 2014). This combined product provides estimates of LWP and IWP, as well as liquid water content (LWC) and ice water content (IWC), although values of IWC in cirrus are underestimated at times due to attenuation by heavy precipitation (Shell et al. 2020). The 30-s product used in this study was averaged into 3-h bins and is available for the period from 10 October 2011 to 8 February 2012. The TropFlux product (Praveen Kumar et al. 2012) provided estimates of surface sensible and latent heat fluxes at daily resolution on a 1° grid. European Centre for Medium-Range Weather Forecasts (ECMWF) operational analysis (OA) used in this study was available at 0.25° horizontal resolution, 20 vertical levels from the surface to 20 hPa, and 6-h intervals. Though not directly used in the analyses in this paper, rainfall estimates from the Tropical Rainfall Measuring Mission (TRMM) 3B42v7 product are shown simply for the purposes of comparison to the other rainfall estimates. This TRMM rainfall product is at 0.25° and 3-h resolution (Huffman et al. 2007).

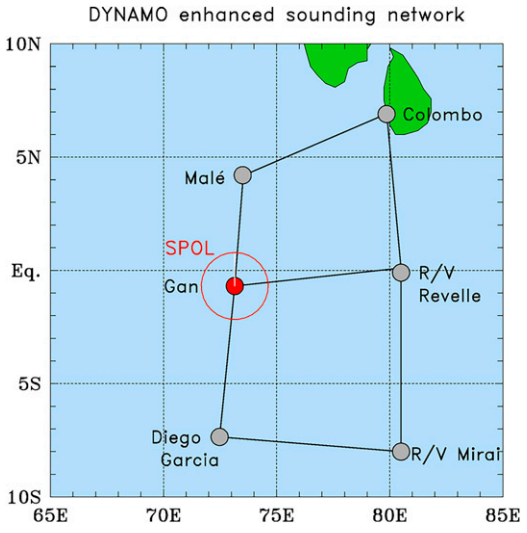

FIG. 1. Map showing the DYNAMO enhanced sounding network. Observations for this study are focused on the Gan Island site (red dot) at 0.69°S, 73.15°E. The outer red circle around Gan indicates the 150-km range ring for the SPOL radar. Budget-estimated rainfall was averaged over this area for comparison to SPOL estimates.

A composite of the three MJOs during DYNAMO was created by applying a low-pass (LP) Kaiser filter (Hamming 1989) in time to retain variability at frequencies 20 days and longer. The composite is constructed in terms of days before and after the time of maximum LP-filtered SPOL rainfall (lag 0). With the application of this filter, 6 days of 3-h data are lost at the ends of the filtered time series (Ciesielski et al. 2017).

b. CBM

In constructing the CBM gridded analyses for this study, ECMWF OA data were used at 5° grid intersections if no observations (soundings, satellite winds, or otherwise) were present within a 4.5° radius of such an intersection. This procedure was used to enhance data coverage outside the main sounding arrays, so results in the interior are largely independent of model analyses and hence parameterizations of physical processes (Johnson et al. 2015). Following interpolation of the OA data to 3-hourly intervals, the sounding data, along with the other observations and model fields described above, were objectively analyzed onto a 1° grid at the surface and at 25-hPa intervals from 1000 to 50 hPa over the entire domain shown in Fig. 1 using the multiquadric interpolation procedure as described in Ciesielski et al. (1997). CBM rainfall estimates that are compared to SPOL measurements are based on averages of the grid points that fall within the 150-km radius of the SPOL surveillance area.

The apparent heat source Q_1 and apparent moisture sink Q_2 are computed using the following heat and moisture budget equations of Yanai et al. (1973) written with z as the vertical coordinate:

$$Q_1 \equiv \frac{\partial \overline{s}}{\partial t} + \overline{\mathbf{v}} \cdot \nabla \overline{s} + \overline{w}\,\frac{\partial \overline{s}}{\partial z} = -\frac{\partial(\overline{\rho}_a \overline{w's'})}{\overline{\rho}_a \partial z} + L(\overline{c} - \overline{e}) + \overline{Q}_R, \tag{1}$$

$$Q_2 \equiv -L\left(\frac{\partial \overline{q}_v}{\partial t} + \overline{\mathbf{v}} \cdot \nabla \overline{q}_v + \overline{w}\,\frac{\partial \overline{q}_v}{\partial z}\right) = -L\,\frac{\partial(\overline{\rho}_a \overline{w'q'_v})}{\overline{\rho}_a \partial z} + L(\overline{c} - \overline{e}), \tag{2}$$

where $s = c_p T + gz$ is the dry static energy, q_v is the water vapor mixing ratio, ρ_a is the density of dry air, L is the latent heat of condensation, c is the condensation rate, e is the evaporation rate, Q_R is the radiative heating rate, and overbar refers to a horizontal average. The averaging area for this study is the 150-km range ring around the SPOL radar as shown in Fig. 1. Vertically integrating (1) and (2) from the surface to the tropopause yields the following integral constraints:

$$\langle Q_1 \rangle = LP_0 + \langle Q_R \rangle + S_0, \tag{3}$$

$$\langle Q_2 \rangle = L(P_0 - E_0), \tag{4}$$

where $\langle(\cdot)\rangle = \int_0^{z_T} (\cdot)\overline{\rho}_a dz$, z_T is the height of the tropopause, and $S_0 = (\overline{\rho}_a c_p \overline{w'T'})_0$ and $LE_0 = (L\overline{\rho}_a \overline{w'q'_v})_0$ are the surface sensible and latent heat fluxes, respectively.

Combining (3) and (4) yields

$$\langle Q_1 \rangle - \langle Q_2 \rangle - \langle Q_R \rangle = S_0 + LE_0. \tag{5}$$

Using surface measurements of S_0 and E_0, surface precipitation P_0 can be computed from (4) and column net radiative heating rate $\langle Q_R \rangle$ from (5) and then compared to independent measurements of those quantities in order to determine the reliability of the budgets. However, as discussed in Yanai and Johnson (1993), Ooyama (2001), and Schubert et al. (2018), Eqs. (1) and (2) are only approximations in that they omit storage and advection of hydrometeors, effects of ice processes, and contributions to entropy changes from dry air, water vapor, cloud condensate, and precipitation.

c. *More accurate budget equations*

To begin with, consider the conventional budget Eq. (4) rewritten in the form

$$P_0 = E_0 + \frac{\langle Q_2 \rangle}{L} = E_0 - \int_0^{z_T} \left(\frac{\partial \overline{q}_v}{\partial t} + \overline{\mathbf{v}} \cdot \nabla \overline{q}_v + \overline{w}\,\frac{\partial \overline{q}_v}{\partial z}\right)\overline{\rho}_a dz. \tag{6}$$

This equation is well suited for use with data from a network of radiosonde stations since with an independent estimate of E_0, sounding data provide all fields needed to compute P_0. However, the more accurate form of (6) includes the effects of cloud condensate and falling precipitation (Ooyama 2001; Schubert et al. 2018):

$$P_A = E_0 + \frac{\langle Q_2 \rangle_A}{L} = E_0 - \int_0^{z_T} \left(\frac{\partial \overline{q}_T}{\partial t} + \overline{\mathbf{v}} \cdot \nabla \overline{q}_T + \overline{w}\,\frac{\partial \overline{q}_T}{\partial z}\right)\overline{\rho}_a dz, \tag{7}$$

where $q_T = q_v + q_c + q_r$, q_c is the airborne condensed water (including both liquid q_l and ice q_i), q_r is the precipitating water, and subscript A refers to the more accurate quantities. E_0 is given by the expression in section 2b as long as there is no cloud condensate (fog) at the ground. Subtracting (6) from (7) yields an expression for a more accurate estimate (P_A) of the precipitation rate:

$$P_A = P_0 - \int_0^{z_T} \left(\frac{\partial \overline{q}_H}{\partial t} + \overline{\mathbf{v}} \cdot \nabla \overline{q}_H + \overline{w}\,\frac{\partial \overline{q}_H}{\partial z}\right)\overline{\rho}_a dz, \tag{8}$$

where $q_H \equiv q_c + q_r$ is the hydrometeor contribution to q_T. This equation states that the computed precipitation P_0 may differ from P_A due to local changes in q_H (referred to here as storage effects) and second by advective effects given by the latter two terms in parentheses on the rhs of (8). Concerning storage, when the hydrometer field is increasing, i.e., $\partial q_H/\partial t > 0$, P_0 will overestimate P_A, while the opposite effect is true when the hydrometer field is decreasing ($\partial q_H/\partial t < 0$). Physically, this means that when cloud and precipitation area coverage is increasing, rather than falling out or evaporating, hydrometeors are "stored" in the growing population of clouds and precipitation. Hydrometeor storage can be important on time scales ranging from individual convective systems (Gallus and Johnson 1991) up to, as will be shown here, the time scale of the MJO.

The other complicating factor relates to hydrometeor transport. For example, hydrometeors generated in an averaging volume during a certain time period may be transported out of the volume, precipitating or evaporating elsewhere. Using the expression for the conservation of mass, (8) can be written in flux form:

$$P_A = P_0 - \int_0^{z_T} \left(\frac{\partial \overline{\rho}_a \overline{q}_H}{\partial t} + \nabla \cdot \overline{\rho}_a \overline{q}_H \overline{\mathbf{v}} + \frac{\partial}{\partial z}\,\overline{\rho}_a \overline{q}_H \overline{w}\right) dz. \tag{9}$$

Assuming $\overline{w} = 0$ at the surface and tropopause, (9) becomes

$$P_A = P_0 - \int_0^{z_T} \left(\frac{\partial \overline{\rho}_a \overline{q}_H}{\partial t} + \nabla \cdot \overline{\rho}_a \overline{q}_H \overline{\mathbf{v}}\right) dz. \tag{10}$$

The first term in parentheses in (10) once again refers to hydrometeor storage, while the second term represents hydrometeor transport into or out of the averaging volume. A column-net divergence of hydrometeors has the same effect as increasing hydrometeor storage; namely, it causes P_0 to overestimate P_A. This could occur, for example, at times of deep convection when there is a divergence of ice in the storm-top outflow layer. An investigation of the radial outflow of ice in the tropical tropopause transition layer atop mesoscale convective systems has been carried out by Virts and Houze (2015).

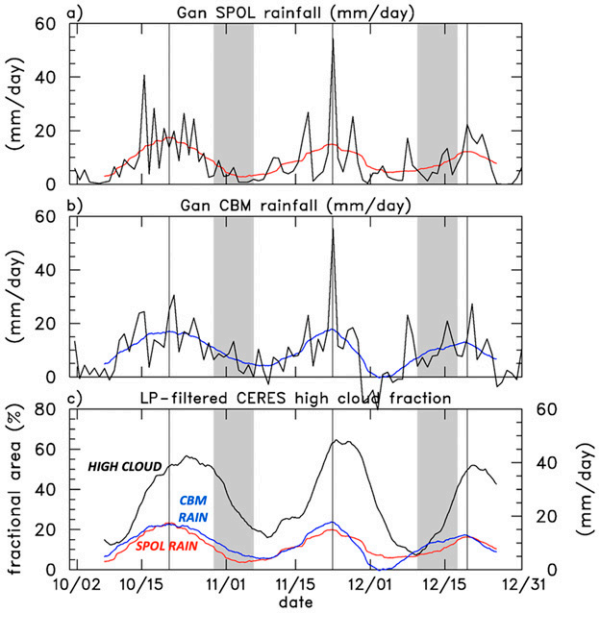

FIG. 2. Time series of (a) daily averaged (black) and LP-filtered (red) SPOL rainfall rate, (b) daily averaged (black) and LP-filtered (blue) budget-estimated rainfall averaged over SPOL radar domain shown in Fig. 1, and (c) CERES LP-filtered high-cloud fraction along with LP-filtered rainfall curves based on SPOL measurements (red) and the conventional budget method (CBM; blue). LP-filtered rainfall peaks for each MJO are indicated by thin vertical lines and time periods when R/V *Revelle* was off station by shading.

Similarly, a more accurate estimate of the column net radiative heating rate $\langle Q_R \rangle_A$ can be obtained from (5), (7), and (10):

$$\begin{aligned}\langle Q_R \rangle_A &= \langle Q_1 \rangle - \langle Q_2 \rangle_A - S_0 - LE_0 \\ &= \langle Q_1 \rangle - LP_A - S_0 \\ &= \langle Q_R \rangle + L\int_0^{z_T} \left(\frac{\partial \overline{\rho}_a \overline{q}_H}{\partial t} + \nabla \cdot \overline{\rho}_a \overline{q}_H \overline{\mathbf{v}} \right) dz. \end{aligned} \tag{11}$$

This result implies that storage of hydrometeors or the divergence of hydrometeors (say, in the convective outflow layer aloft) will lead to an underestimate of the actual column net radiative heating rate (excessive radiative cooling) based on the conventional budget method. While the effects of storage and advection of hydrometeors on budget estimates of radiative heating should, in principle, be discernible, the determination of Q_R as a residual from budgets is a rather sensitive calculation (Johnson and Ciesielski 2000; Johnson et al. 2015) and we have been unable to draw any meaningful conclusions from attempts at such an analysis.

3. Results

Three-month-long time series of daily averaged and LP-filtered rainfall rates based on SPOL and the CBM Q_2 budget are shown in Figs. 2a and 2b. Thin vertical lines in the figure denote the times of the LP-filtered SPOL rainfall peaks

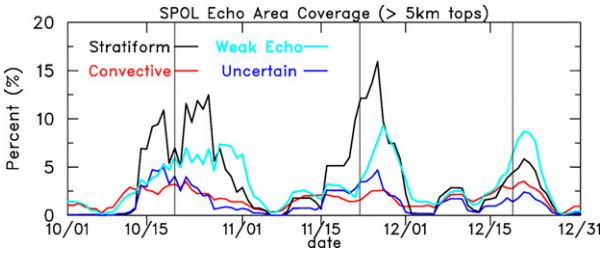

FIG. 3. Time series of 5-day running-mean filtered echo area coverage precipitation categories (with echo tops exceeding 5 km) based on the classification scheme of Powell et al. (2016). Vertical lines indicate times of peak LP-filtered rainfall.

associated with the October, November, and December MJOs. Notable features of the SPOL time series are 1) the prevalence of 2-day peaks that dominate the October MJO rainfall pattern (Zuluaga and Houze 2013; Yu et al. 2018), 2) several large rainfall peaks at ~5-day intervals during the November MJO associated with the passage of Kelvin waves (Moum et al. 2014), and 3) the somewhat weaker amplitude of the December MJO. A comparison of the two LP-filtered rainfall time series is shown in Fig. 2c along with the CERES estimate of high-cloud fraction (HCF) over the SPOL radar domain, used as a proxy for the presence of hydrometers. One to two weeks prior to the peak rainfall for all three MJOs, the CBM rainfall rate exceeds the SPOL rate, while the reverse is true for the decay phases of the November and December MJOs. The different behavior during the decay phase of the October MJO could in part be related to the fact that the R/V *Revelle* was off station during a portion of this period (shading, Fig. 2), causing CBM results to be less reliable.

Another contributing factor, however, in explaining why CBM rain exceeded SPOL rain during late October is the complex evolution of convection that occurred during this period. Figure 3 shows a time series of the area coverage of various precipitation types using the classification methodology described in Powell et al. (2016) for SPOL echoes with tops above 5 km.[1] During late October, the area covered by stratiform precipitation experienced an overall increase followed by a rapid drop-off in the last week of the month. This evolution suggests that a storage of hydrometeors, perhaps aided by a concurrent increase in weak echoes (Fig. 3), could explain at least part of the positive CBM–SPOL difference in late October.

As is evident from Fig. 2b, there is considerable uncertainty in computed daily averaged rainfall (even negative rain at times), largely due to sampling errors associated with sounding array budgets (Mapes et al. 2003). To reduce such errors, averaging in time is required, which is accomplished here by compositing the LP-filtered SPOL and CBM rainfall estimates for the three MJOs as shown in Fig. 4. TRMM rainfall-rate estimates have been included for comparison. CBM

[1] In their procedure, weak precipitation features that have little implication for latent heating are described as "weak echoes" and those that surround convective cores that could not be classified as either convective or stratiform are referred to as "uncertain."

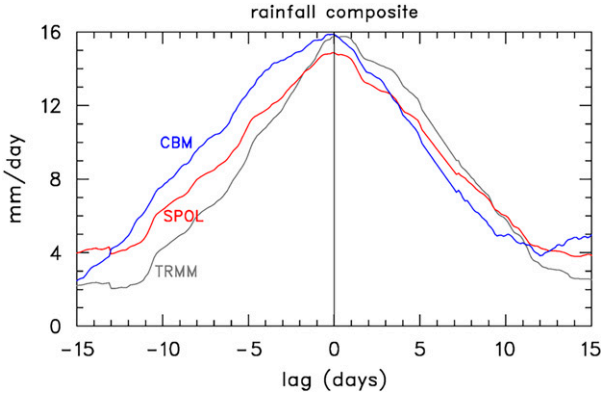

FIG. 4. Three-MJO composite LP-filtered rainfall rates based on SPOL, CBM, and TRMM. Lag 0 refers to the time of maximum LP-filtered SPOL rainfall.

rainfall-rate estimates exceed SPOL estimates by 1–2 mm day^{-1} leading up to the rainfall peak with the reverse being true postpeak, albeit to a lesser extent. This result is consistent with (8), which indicates that budgets should overestimate rainfall rates when the hydrometeor field is increasing and underestimate rainfall rates when the hydrometeor field is decreasing. The TRMM rainfall rates underestimate the SPOL values as convection builds up owing to TRMM undersampling small-scale convection, while TRMM overestimates the rainfall rates in the postpeak stage due to widespread cirrus anvils influencing TRMM estimates (Xu and Rutledge 2014). These deficiencies in the TRMM estimates preclude their use in the rather sensitive analyses of storage and advective effects in thermodynamic budgets.

Possible explanations for the greater CBM rainfall than observed in the MJO buildup phase include 1) the storage of cloud and precipitation as the cloud area expands, and 2) the transport of hydrometeors out of the region, say, in the divergent outflow aloft in deep convection. With respect to storage, we first examine the evolution of the area covered by precipitation. It was already shown in Fig. 2 (lower panel) that greater than 50% of the area was covered by high clouds or cirrus around the time of peak MJO rainfall, and from Fig. 3 that the primary contributors to area coverage for echo tops above 5 km were from stratiform precipitation and weak echoes. To examine echo area coverage by lower clouds, Fig. 5 shows an LP-filtered time series of the fraction of the SPOL radar domain occupied by echoes having reflectivity greater than or equal to a −20-dBZ threshold. There is an increase in cloud coverage (or storage) leading up to the MJO rainfall maxima, followed by ~5–10-day periods of peak area coverage (corresponding to stratiform precipitation) succeeded by a rapid falloff. The SPOL time series does not depict the cirrus area coverage since the minimum sensitivity of SPOL is approximately −25 dBZ at 10-km range. In summary, the time series shown in Figs. 2 and 5 provide qualitative evidence of cloud storage.

To more quantitatively assess the impact of storage, LWP and IWP data from the Gan CombRet product (Feng et al. 2014) are utilized. Figure 6 compares the difference between

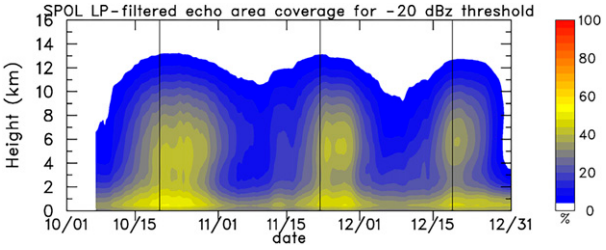

FIG. 5. Time series of LP-filtered −20-dBZ threshold SPOL echo area coverage. Vertical lines indicate times of peak LP-filtered SPOL rainfall.

CBM and SPOL composite rainfall (Fig. 6a) to the liquid, ice, and total water path in the precipitation systems at Gan (Fig. 6b). The yellow range in the top panel represents an uncertainty estimate for the CBM–SPOL difference. It includes 1) a 0.39 mm day^{-1} CBM sampling error (Ciesielski et al. 2021) and 2) SPOL maximum uncertainty estimates as a function of rainfall rate from the DYNAMO Legacy Data Products website (https://data.eol.ucar.edu/project/DLDP), both of which are based on 20-day averages. It can be seen that the difference between the CBM and SPOL rainfall rate estimates lies outside the uncertainty range for a ~10-day period in the MJO developing phases and for a ~3-day period in the weakening phase. The increasing total water path leading up to day 0 and decline afterward (Fig. 6b) are consistent with the idea that storage and removal, respectively, of hydrometeors can help explain the differences between the diagnosed and observed rainfall rates. While this result is qualitatively consistent with expectations regarding hydrometeor storage, the increase of total water path of ~1 mm over the 15-day period leading up to day 0 falls short by at least an order of magnitude in explaining the 1–2 mm day^{-1} budget discrepancy (Fig. 6a).

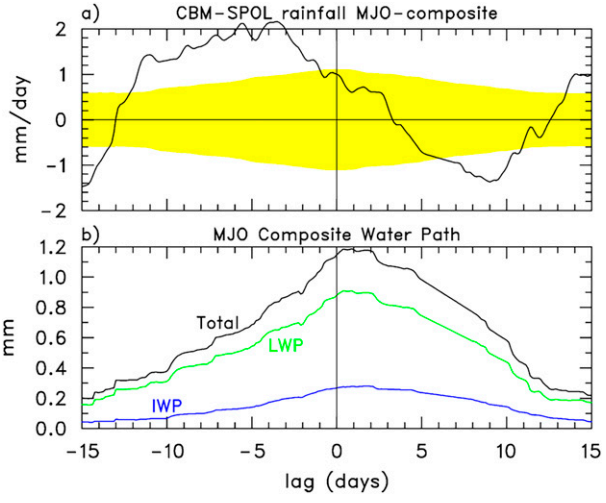

FIG. 6. MJO composite of (a) CBM-minus-SPOL rainfall rate and (b) CombRet-based LWP, IWP, and total water path (LWP + IWP). Yellow shading in (a) represents the uncertainty estimate for the CBM − SPOL rainfall-rate difference.

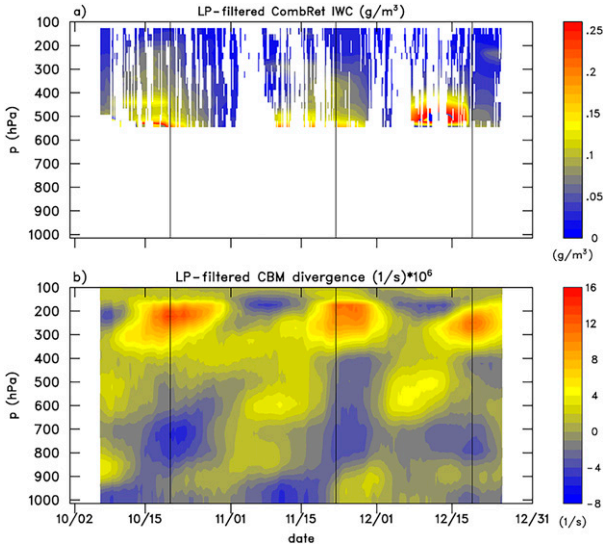

FIG. 7. Time series of LP-filtered (a) CombRet IWC (g m^{-3}) and (b) CBM divergence (10^{-6} s^{-1}) over Gan domain. Vertical lines indicate times of peak LP-filtered rainfall.

Therefore, we next explore the other possible explanation—the transport of hydrometeors out of the region. Satellite imagery of rapidly expanding anvils from individual thunderstorms and mesoscale convective systems suggests that a nonnegligible fraction of hydrometeors generated in a storm region may be exported to distant areas where they subsequently precipitate and/or sublimate. This process is often visually dramatic at midlatitudes where strong updrafts are commonplace. Despite weaker updrafts in tropical convection, it may still be important in the tropics. To estimate this effect, the second term on the rhs of (10) is evaluated using IWC data provided by CombRet and divergence fields from the gridded analysis. Here we make the simplifying assumption that IWC is constant over the SPOL averaging area. Also, we only consider ice transport owing to its slow fall speed relative to liquid. Figure 7 shows LP-filtered time series of both the IWC and divergence over the Gan area, the product of which yields an estimate of the transport.

Strong peaks in divergence occur in the outflow layer near 200 hPa, where the IWC is quite low (<0.1 g m^{-3}). The computed outward transport of hydrometeors integrated over the 150–350 hPa layer is shown in Fig. 8a. Daily average values can at times be large (~0.5 mm day^{-1}; not shown), but the LP-filtered transport reaches only ~0.1 mm day^{-1}. This value, as in the case of storage, is at least an order of magnitude below what is needed to explain the CBM–SPOL rainfall-rate differences (Fig. 8b). It should be noted, however, that the IWC in the outflow layer may frequently be undersampled due to attenuation by intervening deep convective clouds (Shell et al. 2020).

Also shown in Fig. 8a is a time series of the storage term. Despite the low-pass filtering, this term is still quite noisy due to high-frequency convective disturbances that move through the region.

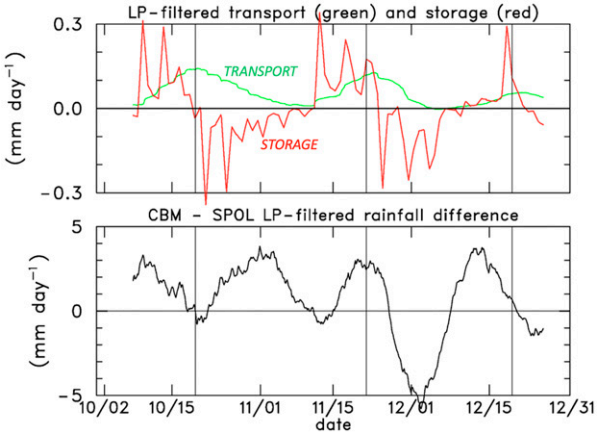

FIG. 8. Time series of LP-filtered (a) hydrometeor export (green) integrated over the 150–350-hPa layer and storage (red) and (b) difference in rainfall rate between the conventional budget method and the SPOL radar (mm day^{-1}). Vertical lines indicate times of peak LP-filtered rainfall.

4. Discussion

The discrepancy between rainfall-rate estimates from sounding-based budgets and radar-based observations, which is related to storage and transport of hydrometeors, appears to be qualitatively explained by our analysis of DYNAMO field campaign data. Namely, remote sensing observations of hydrometeors on Gan Island combined with sounding data yield estimates of storage and advection that are in the right direction with respect to expectations. However, comparing Fig. 9a with Fig. 9b, the estimates for the MJO composite fall short by about an order of magnitude in explaining the discrepancies. The fact that

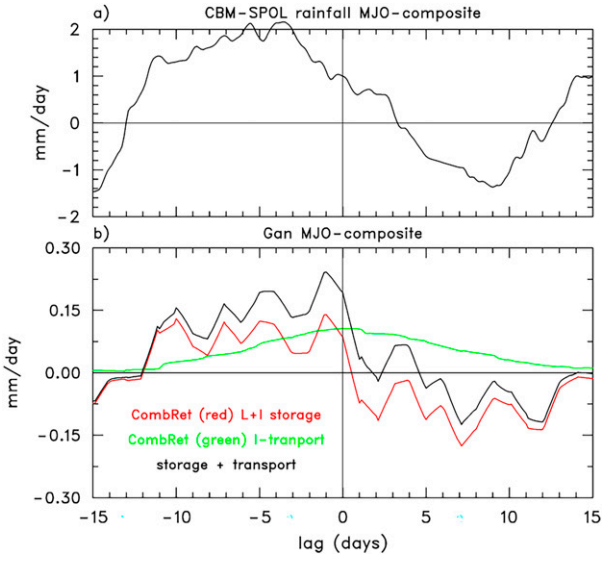

FIG. 9. MJO-composite (a) CBM-minus-SPOL rainfall-rate difference and (b) estimates of hydrometeor storage (red), horizontal transport (green), and the sum of the two (black) for SPOL radar domain based on remote sensing and sounding data.

storage and transport are additive in the growing MJO stage and canceling in the decay stage (Fig. 9b) helps to explain why the magnitude of the CBM–SPOL differences are greater during the former stage than the latter.

Given that the instrumentation deployed in DYNAMO was probably the best suited to date to address the storage and transport issue, our expectations were that the calculations from that campaign would go a long way to explain the budget/radar rainfall-rate estimate discrepancies. Since the results fall short of doing so quantitatively, we conclude that even more sophisticated instrumentation, ideally supported by numerical simulations, and improved sounding network designs will be needed in the future to fully address this problem. An example of the limitations with respect to DYNAMO measurements is the underestimation of the IWC of the high-level cirrus (Shell et al. 2020).

5. Summary and conclusions

Since the pioneering work of Yanai et al. (1973), numerous studies have been carried out to investigate the contributions of convective cloud populations to large-scale heat and moisture budgets using data from atmospheric sounding arrays. The formulations of the conservation equations for heat and moisture used in these studies typically neglect the roles of ice processes as well as the effects of storage and advection of cloud condensate [herein referred to as the conventional budget method (CBM)]. A more accurate treatment of moist thermodynamics introduced by Ooyama (1990, 2001) has been suggested as being appropriate for studies that have the measurement capabilities to evaluate these typically neglected effects (Schubert et al. 2018). Such measurements were available on Gan Island during the 2011 DYNAMO field campaign and they are used in this paper to estimate hydrometeor storage and advection effects on atmospheric budgets. These measurements include the S-band S-PolKa (SPOL) radar and Ka-band cloud radar (KAZR), both deployed on Gan Island, which were merged by Feng et al. (2014) to produce the combined retrieval product referred to as CombRet.

Using the CombRet estimates of ice and liquid water contents and paths, along with the CSU DYNAMO gridded analysis product (Ciesielski et al. 2014), estimates have been made of the storage and advection effects in the thermodynamic budgets. These effects can be interpreted physically in the following way: as the cloud field increases during the developing phase of the MJO, cloud condensate is "stored" in the atmosphere rather than precipitating out immediately. The reverse effect holds true during the decaying phase. In addition, advection in deep convective systems can transport ice hydrometeors into or out of a sampling volume, which can also contribute to errors in traditional budgets that exclude these effects. Equations (8) and (10) contain terms representing these neglected effects.

The results of this study, summarized in Fig. 9, show that storage and advective effects determined from measurements obtained from Gan Island along with sounding gridded analyses are qualitatively consistent with the above expectations. Namely, hydrometeor storage and transport effects cause the CBM method to overestimate rainfall rate in the developing stage of the MJO, with the reverse being true during the decaying stage. However, while the findings are qualitatively consistent with expectations, the estimates of their amplitude fall short by an order of magnitude. To better address this issue, future field campaigns would benefit from denser sounding arrays that yield more accurate budgets, sounding arrays that encircle ground-based remote sensing systems, and improved instrumentation (both ground-based and satellite) that provide more accurate measurements of the content and distribution of hydrometeors in tropical convection.

Acknowledgments. The authors greatly appreciate the constructive comments and suggestions of three anonymous reviewers. We also thank Zhe Feng for his helpful comments. This research has been supported by the National Science Foundation under Grants AGS-1853633 (RHJ) and AGS-1841326 (WHS).

Data availability statement. The CERES cloud and microphysical data were obtained from http://ceres.larc.nasa.gov/products.php?product=SYN1deg, the CombRet cloud microphysical data from https://www.arm.gov/data/pi/71, the SPOL legacy radar data from https://data.eol.ucar.edu/project/DLDP, the TRMM rainfall data from https://disc.gsfc.nasa.gov/datasets/TRMM_3B42_7/summary, the TropFlux surface fluxes from https://incois.gov.in/tropflux/tf_products.jsp, and the CBM gridded diagnosed fields from https://data.eol.ucar.edu/dataset/347.240.

REFERENCES

Ciesielski, P. E., L. Hartten, and R. H. Johnson, 1997: Impacts of merging profiler and rawinsonde winds on TOGA COARE analyses. *J. Atmos. Oceanic Technol.*, **14**, 1264–1279, https://doi.org/10.1175/1520-0426(1997)014<1264:IOMPAR>2.0.CO;2.

——, and Coauthors, 2014: Quality controlled upper-air sounding dataset for DYNAMO/CINDY/AMIE: Development and corrections. *J. Atmos. Oceanic Technol.*, **31**, 741–764, https://doi.org/10.1175/JTECH-D-13-00165.1.

——, R. H. Johnson, X. Jiang, Y. Zhang, and S. Xie, 2017: Relationships between radiation, clouds, and convection during DYNAMO. *J. Geophys. Res. Atmos.*, **122**, 2529–2548, https://doi.org/10.1002/2016JD025965.

——, ——, S. Tang, Y. Zhang, and S. Xie, 2021: Comparison of conventional and constrained variational methods for computing large-scale budgets and forcing fields. *J. Geophys. Res. Atmos.*, **126**, e2021JD035183, https://doi.org/10.1029/2021JD035183.

Feng, Z., S. A. McFarlane, C. Schumacher, S. Ellis, J. Comstock, and N. Bharadwaj, 2014: Constructing a merged cloud–precipitation radar dataset for tropical convective clouds during the DYNAMO/AMIE experiment at Addu Atoll. *J. Atmos. Oceanic Technol.*, **31**, 1021–1042, https://doi.org/10.1175/JTECH-D-13-00132.1.

Gallus, W. A., and R. H. Johnson, 1991: Heat and moisture budgets of an intense midlatitude squall line. *J. Atmos. Sci.*, **48**, 122–146, https://doi.org/10.1175/1520-0469(1991)048<0122:HAMBOA>2.0.CO;2.

Gottschalck, J., P. E. Roundy, C. J. Schreck, A. Vintzileos, and C. Zhang, 2013: Large-scale atmospheric and oceanic conditions during the 2011–12 DYNAMO field campaign. *Mon. Wea. Rev.*, **141**, 4173–4196, https://doi.org/10.1175/MWR-D-13-00022.1.

Hamming, R. W., 1989: *Digital Filters*. Dover, 284 pp.

Huffman, G. J., R. F. Adler, D. T. Bolvin, G. Gu, E. J. Nelkin, K. P. Bowman, E. F. Stocker, and D. B. Wolff, 2007: The TRMM Multisatellite Precipitation Analysis: Quasi-global, multiyear, combined-sensor precipitation estimates at fine scale. *J. Hydrometeor.*, **8**, 33–55, https://doi.org/10.1175/JHM560.1.

Johnson, R. H., 1980: Diagnosis of convective and mesoscale motions during phase III of GATE. *J. Atmos. Sci.*, **37**, 733–753, https://doi.org/10.1175/1520-0469(1980)037<0733:DOCAMM>2.0.CO;2.

——, and P. E. Ciesielski, 2000: Rainfall and radiative heating rate estimates from TOGA COARE atmospheric budgets. *J. Atmos. Sci.*, **57**, 1497–1514, https://doi.org/10.1175/1520-0469(2000)057<1497:RARHRF>2.0.CO;2.

——, ——, J. H. Ruppert Jr., and M. Katsumata, 2015: Sounding-based thermodynamic budgets for DYNAMO. *J. Atmos. Sci.*, **72**, 598–622, https://doi.org/10.1175/JAS-D-14-0202.1.

Madden, R. A., and P. R. Julian, 1971: Detection of a 40–50 day oscillation in the zonal wind in the tropical Pacific. *J. Atmos. Sci.*, **28**, 702–708, https://doi.org/10.1175/1520-0469(1971)028<0702:DOADOI>2.0.CO;2.

Mapes, B. E., P. E. Ciesieslki, and R. H. Johnson, 2003: Sampling errors in rawinsonde-array budgets. *J. Atmos. Sci.*, **60**, 2697–2714, https://doi.org/10.1175/1520-0469(2003)060<2697:SEIRB>2.0.CO;2.

McNab, A. J., and A. K. Betts, 1978: A mesoscale budget study of cumulus convection. *Mon. Wea. Rev.*, **106**, 1317–1331, https://doi.org/10.1175/1520-0493(1978)106<1317:AMBSOC>2.0.CO;2.

Moum, J. N., and Coauthors, 2014: Air–sea interactions from westerly wind bursts during the November 2011 MJO in the Indian Ocean. *Bull. Amer. Meteor. Soc.*, **95**, 1185–1199, https://doi.org/10.1175/BAMS-D-12-00225.1.

Ooyama, K. V., 1990: A thermodynamic foundation for modeling the moist atmosphere. *J. Atmos. Sci.*, **47**, 2580–2593, https://doi.org/10.1175/1520-0469(1990)047<2580:ATFFMT>2.0.CO;2.

——, 2001: A dynamic and thermodynamic foundation for modeling the moist atmosphere with parameterized microphysics. *J. Atmos. Sci.*, **58**, 2073–2102, https://doi.org/10.1175/1520-0469(2001)058<2073:ADATFF>2.0.CO;2.

Peixoto, J. P., and A. H. Oort, 1992: *Physics of Climate*. American Institute of Physics, 520 pp.

Powell, S. W., R. A. Houze Jr., and S. R. Brodzik, 2016: Rainfall-type categorization of radar echoes using polar coordinate reflectivity. *J. Atmos. Sci.*, **33**, 523–538, https://doi.org/10.1175/JTECH-D-15-0135.1.

Praveen Kumar, B., J. Vialard, M. Lengaigne, V. S. N. Murty, M. J. McPhaden, M. F. Cronin, F. Pinsard, and K. Gopala Reddy, 2012: TropFlux wind stresses over the tropical oceans: Evaluation and comparison with other products. *Climate Dyn.*, **40**, 2049–2071, https://doi.org/10.1007/s00382-012-1455-4.

Schubert, W. H., P. E. Ciesielski, and R. H. Johnson, 2018: Heat and moisture budget analysis with an improved form of moist thermodynamics. arXiv, 1810.11119v1, https://doi.org/10.48550/arXiv.1810.11119.

Shell, K. M., S. P. de Szoeke, M. Makiyama, and Z. Feng, 2020: Vertical structure of the radiative heating rates of the MJO during DYNAMO. *J. Climate*, **33**, 5317–5335, https://doi.org/10.1175/JCLI-D-19-0519.1.

Virts, K. S., and R. A. Houze Jr., 2015: Clouds and water vapor in the tropical tropopause transition layer over mesoscale convective systems. *J. Atmos. Sci.*, **72**, 4739–4753, https://doi.org/10.1175/JAS-D-15-0122.1.

Wielicki, B. A., B. R. Barkstrom, E. F. Harrison, R. B. Lee, G. L. Smith, and J. E. Cooper, 1996: Clouds and the Earth's Radiant Energy System (CERES): An Earth Observing System experiment. *Bull. Amer. Meteor. Soc.*, **77**, 853–868, https://doi.org/10.1175/1520-0477(1996)077<0853:CATERE>2.0.CO;2.

Xu, W., and S. A. Rutledge, 2014: Convective characteristics of the Madden–Julian oscillation over the central Indian Ocean observed by shipborne radar during DYNAMO. *J. Atmos. Sci.*, **71**, 2859–2877, https://doi.org/10.1175/JAS-D-13-0372.1.

——, ——, C. Schumacher, and M. Katsumata, 2015: Evolution, properties and spatial variability of MJO convection near and off the equator during DYNAMO. *J. Atmos. Sci.*, **72**, 4126–4147, https://doi.org/10.1175/JAS-D-15-0032.1.

Yanai, M., and R. H. Johnson, 1993: Impacts of cumulus convection on thermodynamic fields. *The Representation of Cumulus Convection in Numerical Models*, *Meteor. Monogr.*, No. 24, Amer. Meteor. Soc., 39–62, https://doi.org/10.1007/978-1-935704-13-3_4.

——, S. Esbensen, and J.-H. Chu, 1973: Determination of bulk properties of tropical cloud clusters from large-scale heat and moisture budgets. *J. Atmos. Sci.*, **30**, 611–627, https://doi.org/10.1175/1520-0469(1973)030<0611:DOBPOT>2.0.CO;2.

Yoneyama, K., C. Zhang, and C. N. Long, 2013: Tracking pulses of the Madden–Julian oscillation. *Bull. Amer. Meteor. Soc.*, **94**, 1871–1891, https://doi.org/10.1175/BAMS-D-12-00157.1.

Yu, H., R. H. Johnson, P. E. Ciesielski, and H.-C. Kuo, 2018: Observation of quasi-2-day convective disturbances in the equatorial Indian Ocean during DYNAMO. *J. Atmos. Sci.*, **75**, 2867–2888, https://doi.org/10.1175/JAS-D-17-0351.1.

Zuluaga, M. D., and R. A. Houze Jr., 2013: Evolution of the population of precipitating convective systems over the equatorial Indian Ocean in active phases of the Madden–Julian oscillation. *J. Atmos. Sci.*, **70**, 2713–2725, https://doi.org/10.1175/JAS-D-12-0311.1.